Chapter 3

Coexistence of large dielectric constant and strong meta-magnetic state in Eu_2CoMnO_6

3.1 Introduction

The ongoing research on multifunctional materials drives people toward double perovskite (DP) oxides, i.e. $A_2BB'O_6$ (A = rare earth/alkaline cation and B/B' = transition metal cations) [50–54]. The recent studies on various rare-earth-based DP with B sites occupied by Co and Mn, that is R_2CoMnO_6 (R = La to Lu), have received extensive attention owing to their various exciting functional properties, viz., electrical and optical properties, defect-induced modulation of physical properties, tunable magnetization steps, magneto-caloric effect and pyro-current, magneto-resistance, exchange bias, magneto-dielectric effects, Griffiths-like and non-Griffiths-like clustered phase, spin-phonon coupling (SPC), Hopkinson effect, multiferroicity, etc. [13,17,19,27,55–65]. The slight change in rare-earth size in the R_2CoMnO_6 family instigates significant variations in the Co-O-Mn bond length and angle; thus, modifying magnetic and electronic ground states via modification of superexchange (SE) interactions. In these DP oxides, the CoO_6 and MnO_6 octahedral are alternately located at the corners of the lattice. A ferromagnetic (FM) ordering arises due to dominant Co^{2+} and Mn^{4+} SE interactions, where the ordering temperature, T_C, linearly decreases from 204 K (La_2CoMnO_6) to 48 K (Lu_2CoMnO_6) due to the decrease of ionic radii of the rare-earth elements from La to Lu [66]. However, due to the arbitrary distribution of Co & Mn at their sites, anti-ferromagnetic (AFM) ordering also arises owing to Co^{2+}-O^{2-}- Co^{2+}/Mn^{4+}-O^{2-}-Mn^{4+} SE interaction along with the dominant ferromagnetic phase. Moreover, the rare earth ions may lead to additional magnetic ordering at lower temperatures, thus resulting in a moderation of the magnetic properties. For example, in Er_2CoMnO_6, a ferrimagnetic behavior has been seen below 30 K owing to the magnetic ordering of Er^{3+} moments with Co & Mn sub lattice, other than the FM ordering of the Co^{2+} and Mn^{4+} below 70 K [67]. Eu_2CoMnO_6 (ECMO) has been less studied, thus there are more possibilities to explore its electrical and magnetic properties. Previously, Yu Shun Jia *et al.* investigated the magnetic properties and critical behavior of ECMO via the modified Arrott. Plots, the Kouvel-Fisher plot, and the critical isotherm analysis. They found that the reliable value of critical parameters (β, δ, and γ) of ECMO is close to the value of the mean-field theoretical model. Further, J. Krishnamurthy *et al.* reported a magnetic field-induced MMT [67–70], magneto-caloric effect, and Pyro current in ECMO. Our previous study on ECMO also shows a sharp MMT along with Griffiths-like-phase, Spin-frustration/Spin-glass, Hopkinson-effect, and Spin-Phonon coupling. In this report, we have presented the electrical property along with an exploration of the magnetic property ECMO [67].

3.2 Experimental details

The polycrystalline pellets of the Eu_2CoMnO_6 sample were produced via the solid-state reaction route, described in ref. [67].The X-ray diffraction (XRD) pattern was analyzed using FULLPROF suite software and the VESTA software was used to see the 3-dimensional structure. The X-ray absorption spectroscopy (XAS) and X-ray magnetic circular dichroism (XMCD) measurement was performed at BL-14 beam line with polarized X-ray at Hiroshima synchrotron radiation center (HISOR) [71]. The dielectric measurement was performed using a Key sight E4980A Precision LCR meter. Here, the sample is put in the middle of two metallic electrodes, forming a parallel-plate capacitor-type arrangement.

3.3 Results and Discussion

3.3.1 X-ray diffraction study

The DP's R_2CoMnO_6, usually adopt either an orthorhombic phase [71,72] (space symmetry Pnma) where Co/Mn ions are randomly situated over 6c-sites or a monoclinic phase [73,74] (space symmetry P21/n) where Co/Mn cations are occupied 2c and 2d Wyckoff positions in a perfectly ordered manner. However, in the ordered state itself, there is the possibility that some of the Co & Mn cations may exchange their crystallographic sites depending upon variations in sintering temperature heating/cooling rate, valance states, etc. In most of the R_2CoMnO_6 DP's Co is found in Co^{2+}/Co^{3+} mix valance states whereas Mn in Mn^{3+}/Mn^{4+} states due to the very slight difference in redox potentials among Co^{2+}-Mn^{4+} and Co^{3+}-Mn^{3+} couples [75].

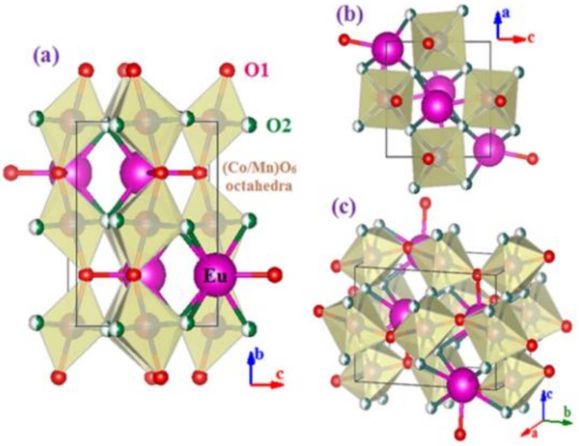

Figure 3.1: *3D structure of ECMO indicating the tilted chains of (Co/Mn) O_6 octahedral along the (a) b-axis, (b) a-axis, and (c) the standard orientation of crystal shape of ECMO unit cell.*

Moreover, the difference in ionic radii between Co^{2+} and Mn^{4+} may cause internal strain and trigger an auspicious mix of valances. Such mixed-valence states in ECMO have already been discussed in ref. [76], where the XRD pattern of ECMO was fitted with an orthorhombic phase (Pnma). Further, no impurity phase was detected. Fig. 3.1 contains the 3D structure of ECMO obtained from VESTA, showing the three-dimensional array of (Co/Mn) O_6 octahedral. From Fig.3.1 (a, b) we can easily see the array of tilted chains of these corner-sharing Octahedral along the crystallographic b & a-axis. Moreover, the standard orientation of the crystal shape of the ECMO unit cell is depicted in Fig. 3.1(c).

3.3.2 X-ray absorption spectroscopy study

As the valance states of Co & Mn are closely connected with their cationic ordering; thus, the study of their electronic structure may support the study of the origins of many features of R_2CoMnO_6 DP's. Other than XPS, the XAS is another supervisory approach for viewing ion's electronic states, spin and orbital magnetic moments, and their interactions with one another. Here an incident X-ray excites electrons from the core level to unoccupied valence levels. The dipole selection principles govern these transitions. It is directly related to the vacant density of states, and hence we can examine several pieces of information regarding oxidation states and magnetic structure [77–79]. Thus, we have measured the XAS spectra of the Co-$L_{2,3}$ & Mn-$L_{2,3}$ edges of ECMO. Fig. 3.2(a) displays the Co-$L_{2,3}$ (XAS spectra collected at 300 K, which is attributed to the electronic transition from the Co2p core to the unoccupied Co3d level). This figure shows that the Co-$L_{2,3}$ XAS spectrum of ECMO is composed of two main intense peaks around 778.9 eV and 794.2 eV. Typically, these peaks are labeled as Co $2p_{3/2}$ (778.9 eV) and Co $2p_{1/2}$ (794.2 eV). The energy difference between these two peaks is called spin-orbit splitting, which is related to the spin and orbital angular momentum of the electrons in the cobalt atom. These peaks are related to the Co^{2+} oxidation state of Co [80,81]. However, it has been analyzed that there are also weak peaks (marked with a green arrow) merged with the main peaks around 781.2 eV (in Co-L_3 spectra) and 796.4 eV (in Co-L_2 spectra). These peaks are seemingly associated with the Co^{3+} oxidation state of Co. This result again confirms a mixed valance state of Co with a dominating Co^{2+} state in ECMO, which is already been observed using the XPS study. Further, the Mn-$L_{2,3}$ edge XAS spectra of ECMO collected at 300 K are displayed in Fig. 3.2(b). It also exhibits two broad spin-orbit splitting features: The Mn $2p_{3/2}$ and Mn $2p_{1/2}$ peaks, which result from the dipole transition from the 2p core to unoccupied 3d levels. Both, Mn $2p_{3/2}$ & Mn $2p_{1/2}$ spectra consist of two clear peaks related to the Mn^{3+}/Mn^{4+} valance state of Mn [57]. Thus, the XAS spectrum also suggests a mixed valence of Mn with dominating Mn^{4+}, which is consistent with the XPS study reported in ref [76].

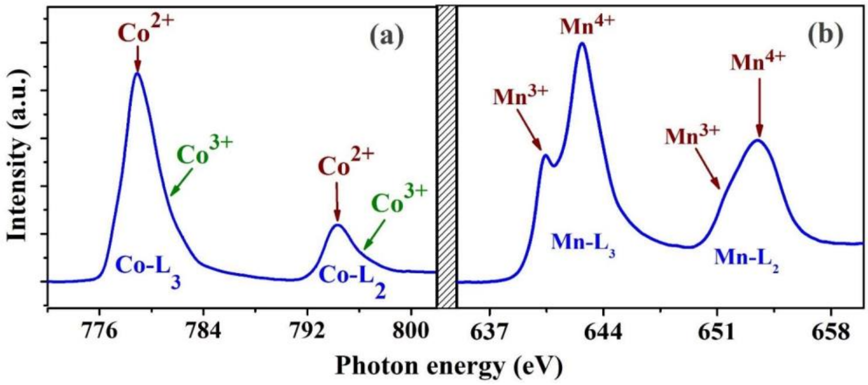

Figure 3.2: *The XAS spectrum of (a) Co $L_{2,3}$ edge and (b) Mn $L_{2,3}$ edge at 300 K.*

3.3.3 Resistivity measurement

Fig. 3.3(a) depicts the electrical resistivity (ρ) *vs.* temperature (T) of ECMO below room temperature. This figure demonstrates that the resistivity increases with decreasing temperature showing a semiconducting manner. Below 200 K temperature, ρ(T) is fitted with the variable range hopping (VRH) model [68,70,82]. The equation relating to the VRH is given as

$$\rho = \rho_0 \exp(\frac{T_0}{T})^{1/4} \tag{10}$$

$$ln\rho = ln\rho_0 + ({T_0}^{1/4}).\,(T^{-1/4}) \tag{11}$$

With $T_0 = \frac{24\alpha^3}{\pi K_B N E_F}$, Where ρ_0 is a perfector, T_0 is the Mott's characteristics temperature, α is the inverse of the localization length of the wave function, k_B is the Boltzmann constant, and $N(E_F)$ is the localized density of states near the Fermi level. The fitting of equation (10) (left inset of Fig. 3.3(a)) gives the numerical values of T_0. The 1/α is around twice the Co-Mn bond [67], which is ~ 3.88×10^{-10} m [70] for ECMO. In La_2CoMnO_6, Rabindra *et al.* assumed the value of 1/α of ~10^{-10} m. The activation energy of Polaron (W) at any temperature T is given by

$$W = \frac{1}{4} \left(K_B T_0^{1/4} T^{3/4} \right) \tag{12}$$

and the most possible hopping distance,

$$R = \left[\frac{9}{8\Pi\alpha K_B N E_F}\right]^{1/4} = \left[\frac{9T_0}{192\alpha^4}\right]^{1/4} \tag{13}$$

The estimated value of $N(E_F)$ for ECMO near the Fermi level is ~10^{24} eV-m^{-3}, the order of a typical semiconducting oxide [70]. According to Mott criteria of the VRH model, We should be greater than thermal energy (k_BT) and R should be such that αR > 1 [82]. Table 1 summarizes the different VRH parameters of ECMO signifying the validity of Mott's criteria. At temperatures above 200 K the *ρ(T)* best follows a thermally activated small polaron hopping (SPH) [69,83], due to an increase in drift mobility and hopping frequency of the carriers. In SPH, ρ(T) follows the equation.

$$\rho = \rho_0 T exp^{\frac{E_a}{TK_B}} \tag{14}$$

From the SPH fitting (right inset of Fig. 3.3(a)), the polaron activation energy (Ea) was found to be around 0.145 eV for ECMO. From UPS, it has been observed that there are no finite electronic states around the Fermi level (E_F), showing the insulating/semiconducting nature of the system. Interestingly, temperature-dependent electrical resistivity also shows the semiconducting nature of ECMO. Two successive valance bands (V. B.) maxima have been observed below the Fermi level at 1.0 eV and 2.4 eV respectively. Further from the UV-visible spectrum, we have observed two successful. The absorption edge of 2.3 eV and 3.7 eV respectively. Using these data, we have drawn a typical Electronic-level diagram of ECMO, which is presented in Fig. 3.3(b).

Table1: VRH parameters for ECMO.

Sample	**$T_0^{1/4}$ (K)**	**N(E_F) ($eV^{-1}m^{-3}$)**	**W @200 K (eV)**	**αR**
ECMO	164.19	1.90×10^{24}	0.188	76.40

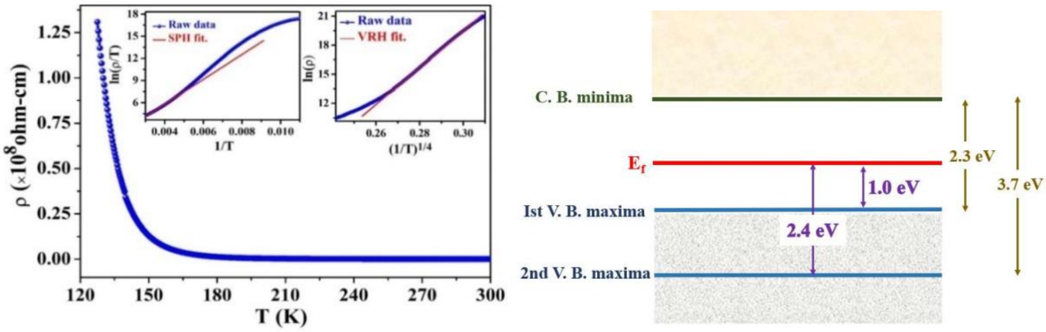

Figure 3.3 *(a) The ρ-T curve of ECMO with insets showing VRH and SPH fitting. (b) Systematic diagram of band gap energies.*

3.3.4 Dielectric measurement

The temperature-dependent dielectric constant (ε′) of ECMO in the range of 10-325 K at different frequencies, calculated from the electric capacitance measurement is shown in Fig. 3.4(a). The curves show an almost non-dispersive intrinsic polarization nature below 160 K with ε′ (T) ~ 90 to 110 symptomatic of the electric dipole relaxation freeze out and did not follow the applied AC electric signal. Above 160 K, it increases sharply showing a step like nature. Amusingly below 160 K with ε′ (T) ~ 90 to 110 symptomatic of the electric dipole relaxation freezes out and does not follow the applied AC electric signal. Besides this, an increase in frequency shifts the step position toward the higher temperature. Such strong frequency dispersion of ε′ near room temperature is ascribed to extrinsic polarization probably owing to the Maxwell-Wagner (MW) effect assisted by electron’s depletion layers amongst samples and contacts or at grain boundaries [73,74,84–86]. In a sister compound LCMO, it has been ascribed that the electrically mixed microstructure which is composed of some conducting regions (as a result of ASD) and insulating regions (due to perfect Co/Mn ordering), might be a reason behind the high value of room temperature dielectric constant [74].

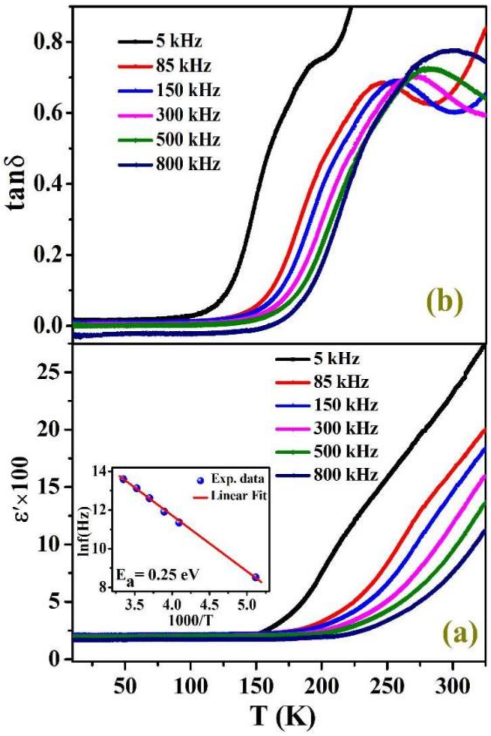

Figure 3.4: *(a) The ε' vs. T and (b) $\tan(\delta)$ vs. T of ECMO at different frequencies. The inset of (a) displays the Arrhenius law fitting for the relaxation peaks.*

The steps, showing a transition from intrinsic to the extrinsic region are associated with a peak in dielectric loss i.e., $\tan(\delta)$ curves (Fig 3.4(b)). The measured peak temperature of $\tan(\delta)$ at measuring frequencies is illustrated in the inset of Fig. 3.4(a). The shifting of $\tan(\delta)$ -peak towards higher temperature for higher frequency (f) is a sign of a thermally activated relaxation phenomenon, which obeys the Arrhenius law,

$$f = f_0 \exp\left[\frac{-E_a}{k_B T}\right] \tag{15}$$

Where $1/f_0 = \tau_0$ is the relaxation time of the dipoles and Ea is the energy required for reorientation of the dipolar region known as activation energy. The fitting of equation (15) for ECMO results in activation energy ~ 0.25 eV with a relaxation time of ~10^{-10} seconds.

3.3.5 Impedance measurement and Cole- Cole plot

As discussed, the dielectric relaxation in ECMO is attributed to non-Debye/MW polarization where the materials do not pass using any permanent dipole moment [87]. The electric polarization arises owing to interfacial depletion layers of carrier amongst sample & contact and at the grain boundaries. The frequency-dependent properties of complicated oxides are generally analyzed using complex functions such as impedance (Z) study. Fig 3.5 shows the Cole-Cole plot (Z′ *vs.* Z″) of ECMO at different temperatures. The figure shows the presence of a semicircular arc. The observed diameters of these semicircles increase on lowering the temperatures. This is the signature of thermally activated conduction and suggests a semiconducting characteristic of the ECMO sample [53]. The complex impedance study has also been employed to compare the micro-structural contribution to the electrical properties of the materials, using an electrical equivalent circuit ascribed to intergranular/grain-boundary resistance and capacitance [87,88].

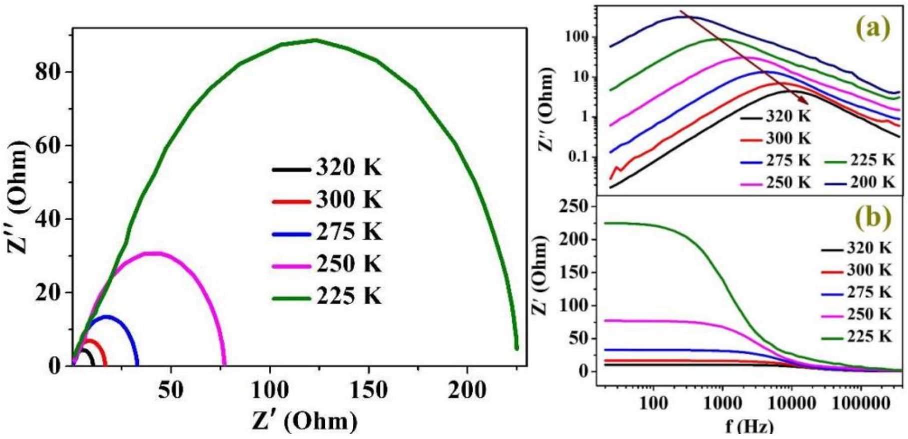

Figure 3.5: *Cole-Cole plot of ECMO at different temperatures. (a) Shows the Z″ vs. f*

curves at a few selected temperatures and (b) Z″ vs. f curves shoes relaxation peaks at different temperatures.

The lower frequency side peak corresponds to the electrical responses of grain boundary and that of the peaks observed at the higher frequency side corresponds to electrical responses of grain conduction while intensities of the relaxation peaks are proportional to the resistances of grain boundaries and grains. Thus, the impedance circuit of the system is considered a series combination of two resistances (R) and two capacitances (C) connected in parallel, attributed to grain (G) and grain boundary (GB) contributions. In this scenario, the Z″-dispersion is given as [87,88],

$$Z'' = R_g\left[\frac{2\text{п}R_gC_g}{1+\left(2\text{п}R_gC_g\right)^2}\right] + R_{gb}\left[\frac{2\text{п}R_{gb}C_{gb}}{1+\left(2\text{п}R_{gb}C_{gb}\right)^2}\right] \qquad (16)$$

The grains and grain boundaries relaxation peak is situated at frequency f= $1/2\text{п}R_gC_g$ and $1/2\text{п}R_{gb}C_{gb}$. Respectively the intensity of the peak will be equal to $R_g/2$ and $R_{gb}/2$. However, for ECMO, the Z″-dispersion curve shows only one relaxation peak (shown with an arrow) within the measured frequency range. The other peak is not observed in the measured frequency range. This relaxation peak moves towards the higher frequencies and peak intensity decreases with increasing temperature, again indicating that the electrical responses are thermally activated with a semiconducting nature. Fig. 3.5(b) shows the variation of the real part of impedance (Z′) with the frequency of ECMO at different temperatures. These curves show that at lower frequency Z′ has a high value at low frequency and temperature. The magnitude of Z′ decreases with increasing frequency and temperature. This behavior is attributed to the enhanced mobility of carriers and the lowering of the density of trapped charges. The merging of Z′ at a higher frequency corroborates the accumulation of space charge in the system [89].

3.3.6 Magnetic measurement

Fig. 3.6(a) illustrates the conventional ZFC (zero fields cooled) and FC (field cooled) magnetization (M) *vs.* T curves of ECMO with 100 Oe applied fields. These curves show an abrupt change in magnetization below 125 K (T_C), showing the commencement of long-range magnetic ordering in the sample. The bifurcation amongst the ZFC/FC curves suggests the presence of spin frustration in the system. Also, the ZFC-M of the ECMO shows a narrow maximum just below T_C with a cusp at a temperature of around 123.2 K (T_a) at 100 Oe (Fig 3.6(a)). Further, these maxima grow to broaden at the higher field (Fig. 3.6(b)) and display a plateau-like nature. Such behavior arises owing to the opposition between local magnetic anisotropy and external magneto-static energy. To explicate the behavior of the paramagnetic state in the high-temperature ($T > T_C$) region, we have presented the inverse susceptibility (χ^{-1}) *vs.* T at H = 100 Oe in the inset of Fig 3.6 (b). The downturn deviation of the experimental value of χ^{-1}(T) in the temperature range $T_C < T < T_G$ is the violation of the usual Curie–Weiss (CW) law of the paramagnetic phase. Such behavior is related to a well-known phenomenon, i.e., Griffiths phase. In this region, the χ^{-1}(T) follows power-low behavior given by,

$$\chi^{-1}(T) = A[(T/T_C^R) - 1]^{1-\lambda} \tag{17}$$

This equation is described in detail in our earlier report [50,90]. The exponent λ lies between 0 to 1 for $T_C^R < T < T_{GP}$. For ECMO, the value of λ is found to be around 0.47 fit in the GP region (as shown in the inset of Fig. 3.6((a)), which again confirms the presence of the Griffiths phase. However, for $T > T_C$, χ^{-1}(T) varies linearly according to CW law, $\chi = C/(T-T_{CW})$, showing a pure PM phase. An anomalous behavior has been observed in the thermal evolution of the ZFC-M, i.e., one can notice that at low field values (H = 100 Oe) becomes negative on decreasing temperature below T_a down to a certain temperature T_{CMOP} (compensated temperature) and remains negative for all $T < T_{COMP}$. Further, from Fig. 3.6(b) it has been observed that such negative magnetization in the ZFC curve has also been observed at a few higher fields (H = 1 kOe and 10 kOe). However, in other higher fields, it becomes completely positive Fig .3.6(b).

Similar negative behavior has been observed by Mazumdar *et al.*, in DP's Ho_2CoMnO_6. They reported that a negative 3d–4f exchange interaction amongst the PM moment of Ho^{3+}ions and the FM moment of the Co^{2+}-Mn^{4+} sub lattice is a possible reason behind such uncommon negative magnetization in Ho_2CoMnO_6.Thus, it can be elucidated that the negative 3d–4f exchange interaction between the PM moment of Eu^{3+}ions and the FM moment of the Co^{2+}-Mn^{4+} unit may originate such uncommon negative magnetization in ECMO. Other than this, local anti-site disorder (ASD) plays a significant role in realizing the negative ZFC-M. Due to the presence of ASD at the Co/Mn sites, an anti-phase boundary (APB) has been realized in such a system. At APBs, the short-range FM Co^{2+}-O^{2-}-Mn^{4+} clusters/domains get anti-ferromagnetically coupled strongly. In ZFC mode, the spins get frozen at lower temperatures with anti-ferromagnetic (AFM) coupling. A sufficiently higher magnetic field is required to break the AFM coupling at lower temperatures. Thus, the application of a relatively low magnetic field cannot overwhelm the AFM coupling strength of FM clusters at APBs, hence giving rise to a net negative magnetization in the system. However, the sufficient higher applied field (e.g., at $H > 1$ kOe for Ho_2CoMnO_6 [17] and $H > 10$ kOe for Eu_2CoMnO_6) causes a positive ZFC-M over the measured temperature range by decoupling the FM domains at APB's. Another interesting magnetic property observed in ECMO is a step-like jump (i.e., meta-magnetic transition) in the low-temperature isothermal magnetization *vs.* magnetic field curve (Fig. 3.7(a)). The coexistence of FM and AFM coupling of Co and Mn ions along with APBs due to the presence of ASD is the main reason behind the origin of steps in isothermal magnetization.

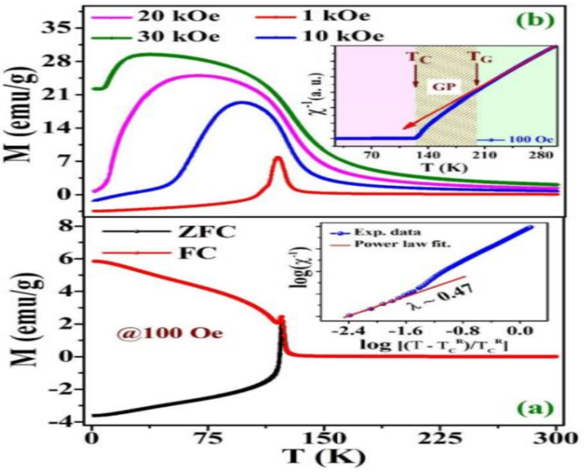

Figure 3.6: *(a) The ZFC/FC magnetization vs. T with inset showing power law fitting. (b) The variation of ZFC Magnetization vs. T at different fields with inset showing* $\chi(T)$ *curve of ECMO.*

To get supplementary information concerning the coupling of magnetic moments of Co and Mn ions in ECMO we have carried out XMCD.

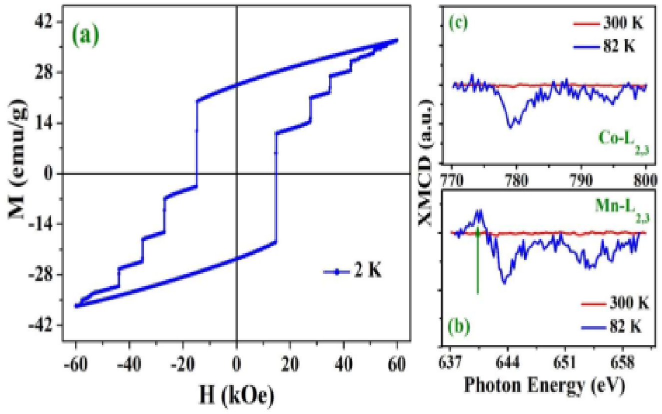

Figure 3.7 *(a) M vs. H curve (b) Mn-*$L_{2,3}$ *XMCD spectra (c) Co-*$L_{2,3}$ *XMCD spectra of ECMO.*

Fig. 3.7(c) consists of Co$L_{2,3}$ XMCD spectra and Fig 3.7(b) consists of Mn-$L_{2,3}$ XMCD spectra taken at two different temperatures, i.e., 300 K (paramagnetic state) and 82 K (below ordering temperature). For this, we have taken the difference of two XAS spectra whose measurement was made with circularly polarized x-rays under the application of ±1 Tesla magnetic field. We did not observe any XMCD signal at 300 K for both ions, which is consistent with the paramagnetic behavior of ECMO. But we can observe a significant XMCD signal at the L_3-edge at 82 K. From XMCD spectra (at 82 K) we can see that most of the signals are of the same polarity. Thus, most of the magnetic moment of Co is aligned in parallel to that of Mn at 82 K resulting in the FM behavior of ECMO at lower temperatures. Further, a small XMCD signal of opposite polarity confirms AFM coupling around 640 eV at the Mn-L_3 edge (shown by an arrow in Fig. 3.7(b)) [80,90,91]. Hence, these are consistent with the expected results from the magneto-meter that there exist anti-ferromagnetically coupled FM domains.

3.4 Conclusion

The polycrystalline Eu_2CoMnO_6 prepared through the solid-state reaction method, crystallized in a single orthorhombic phase (Pnma space symmetry). The transition metal cation has been found in a mixed valance state [Co (2+/3+) and Mn (3+/4+)] in this system, confirmed by both XPS and XAS studies. The thermal variation of resistivity measurement has been fitted with VRH and SPH models and suggests a semiconducting nature of Eu_2CoMnO_6. The dielectric spectrum shows a strong frequency dispersion and Maxwell-Wegner-type polarization with a large dielectric constant. The accumulation of space charge in the system has been confirmed by the impedance spectrum. The Cole-Cole plot and imaginary part of impedance show thermally activated electrical conduction and the semiconducting nature of Eu_2CoMnO_6. The real part of impedance shows a high value at low temperatures and frequency while it decreases at higher temperatures and frequency due to the increased mobility of charge carriers at higher temperatures. The magnetization measurement shows that the system enters into a magnetically ordered region below 125 K followed by a short-range FM clustered phase (Griffiths-like phase). Moreover, there exist competing FM and AFM phases due to mixed valance states of Co/Mn cations. Moreover, Eu_2CoMnO_6 has a strong meta-magnetic state due to the presence of antisite disorder and AFM coupling at the anti-phase boundary.